J MATER SCI **41** (2006) 2711–2722

# Insights into nanoparticle formation mechanisms

C. R. PERREY, C. B. CARTER*
*Department of Ch. E. & Materials Science, University of Minnesota, Minneapolis, MN 55455*
*E-mail: cbcarter@umn.edu*

**Published online:** 17 April 2006

Nanoparticles and nanoparticle-based devices are of interest in numerous industrial applications due to their unique and often advantageous properties. However, a major obstacle to the full exploitation of nanoscale materials is the lack of production processes that yield specific materials reproducibly. A fundamental understanding of nanoparticle formation in candidate production systems is critical to achieving both product specificity and uniformity. The present work uses observations from transmission electron microscopy to elucidate the formation processes occurring for silicon and titanium nanoparticles produced from a thermal plasma process. The structure, chemistry, and defect morphology of the nanoparticles are consistent with a rapid cooling and crystallization from a liquid droplet. The observation of surface faceting on some nanoparticles suggests a transition between different crystalline growth regimes. 

## 1. Introduction

Research has shown that materials with dimensions on the 1 to 100 nm length scale can exhibit properties which differ from those of the same macroscopic material [1–3]. One such example of this phenomenon is Si nanoparticles which have been shown to have a much greater hardness than bulk Si [4–6]. Related results have been found for optical [7], electronic [8], magnetic [9, 10], chemical [11], and structural properties [12–15]. These discoveries suggest innumerable new potential devices and applications that utilize these modified properties [2]. Particles in this size range have been referred to as "superfine" [1, 16], "very small" [17–19], and most recently, including here, as "nanoparticles" [20, 21].

One of the major difficulties with the incorporation of nanostructured materials into industrial applications is the production of such materials. The design and operation of systems that produce a chemically and structurally specified material at a low cost is a challenge for the field of nanotechnology. Among the gas-to-particle routes, thermal plasma-based processes offer such an opportunity in the high-rate production of nanostructured materials [22, 23]. However, these systems are complicated and not well understood, often producing materials with a large degree of agglomeration or chemical impurities [24–29]. Since the structure and morphology of the nanoparticles is critical to the observed properties a better understanding of the processing–structure relationship is necessary.

A full theoretical description of the aerosol dynamics of a plasma process is very complex due to the presence of both neutral atoms and ions, large temperature gradients, and different possible chemical reactions [30, 31]. A general solution for such a system would require solving Maxwell's equations, the Navier–Stokes equations, and the equations describing the aerosol dynamics [16]. For example, once particles are nucleated they may undergo a number of processes, including condensation, coalescence (sintering), coagulation, and agglomeration. These processes are a function of pressure, particle concentration, temperature, and the residence times in the production apparatus. Additionally, the material properties may be a complex function of these variables; an example is the various diffusion coefficients for the particles [32–35]. There are other relations between these factors; coalescence of two liquid nanoparticles is often an exothermic process which can raise the temperature of the aggregate nanoparticle [36]; the total surface energy of the particle is reduced. Work involving Si-particle formation has shown that particle sintering and morphology are especially sensitive to temperature and cluster size [37]. Other work has focused on the influence of the reactor formation conditions on structure and morphology [35, 38–45].

*Author to whom all correspondence should be addressed.
0022-2461 
DOI: 10.1007/s10853-006-7874-z

The rapid solidification of materials has long been of interest, both scientifically and technologically. Such non-equilibrium processes can yield materials with novel crystalline or amorphous phases and extended solid solubility [46]. Experiments using millimeter-sized droplets of Si [47], Ge [48–56], Ni [57], Ga [46, 58, 59], Al [60, 61], and metallic alloys [46, 49, 62] have shown that the extent of supercooling determines the shape of the solid/liquid interface (the "crystallization front", CF), as it propagates into the liquid [59, 63]. At small undercoolings a lateral-growth mechanism dominates, where the CF is faceted and crystal growth proceeds by the propagation of these facets [63]. However, at large undercoolings the CF becomes rough and atomic attachment occurs isotropically along the boundary. This regime is termed "continuous growth."

An experimental approach focusing on the observation of the product material is necessary for both verification of theoretical assumptions and control of the plasma-based nanoparticle production apparatus. Characterization of the chemistry, structure, and size distribution of the nanoscale materials is required to understand the processing–property relationships that make these materials uniquely desirable for industrial applications. The inherently small size of the particles produced makes the use of transmission electron microscopy (TEM) a necessity. The TEM can yield information on the chemistry, bonding and structure at the atomic level while providing important information about other items of interest, such as the size distribution and morphology of the constituent nanoparticles [64]. In this study, TEM observations of nanoparticles of Si and Ti are used to give further insight into nanoparticle-formation processes in a thermal plasma.

## 2. Experimental

Nanoparticles were created using hypersonic plasma particle deposition (HPPD), a process described in detail elsewhere [6, 65–70]. In the HPPD technique, vapor-phase precursors are injected into a thermal plasma generated by a DC arc torch. The plasma is quenched as it is expanded through a nozzle; the resulting nanoparticles are then focused using an aerodynamic lens system [71, 72]. This series of lenses focuses the nanoparticles into a narrow beam with a width of a few tens of microns [73]. A motorized deposition platform allows the translation of a substrate through this nanoparticle beam, thus patterning the substrate. For the present study, ultrathin carbon TEM support films (SPI Supplies) were translated through the nanoparticle beam, creating a "line" of nanoparticles across the support film. This method was used to deposit nanoparticles of Si and Ti on TEM support films for observation.

Different TEMs were used to analyze the specimens. Conventional TEM examination of the nanoparticles was carried out using a Philips CM30 operating at an accelerating voltage of 300 kV. High-resolution imaging used the spherical aberration-corrected Philips CM200 FEG-TEM at Jülich [74–82], a Philips CM300 FEG-TEM at the National Center for Electron Microscopy in Berkeley, CA [83], and a FEI Tecnai F30 FEG-TEM. The CM300 is equipped with a GIF and has a spherical aberration constant ($C_S$) of 0.65 mm, while the images from the aberration-corrected CM200 were recorded with a coma of below 73 nm and setting $C_S$ to approximately $-40\ \mu$m [75, 84, 85].

## 3. Results

A representative individual Si particle is shown in the BF TEM image of Fig. 1a. The spherical shape of the particle can appreciated from the nearly circular shape in this projection and the fact that the thickness fringes also appear as circular contours. The single-crystal nature of this nanoparticle is confirmed by the selected-area diffraction (SAD) pattern in Fig. 1b. This pattern is consistent with the [011] zone axis of Si. A HRTEM image of the surface of a similar nanoparticle (Fig. 1c) shows the existence of a thin amorphous layer surrounding the nanoparticle; the thickness fringes again follow the contour of the surface. This layer has been identified as an oxide layer using electron energy-loss spectrometry [86, 87].

Twin boundaries are commonly observed in these Si nanoparticles. Fig. 2 is a HRTEM image along the [011] direction showing two parallel (111) twin boundaries. These two interfaces are separated by approximately 2.5 nm, and appear to be atomically flat. The surface of the nanoparticle between the two twin boundaries appears to be more angular than that of the surrounding area. This behavior is also seen for more closely spaced twin boundaries. Fig. 3 shows an array of nine parallel (111) twin boundaries that are irregularly spaced. The surface of the Si nanoparticle appears to have (111)-type nanofacets for each enclosed twin domain. Again, the twin boundaries are all atomically flat along the length of the interface and extend across the particle.

Some nanoparticles observed are not completely crystalline; such a particle is shown in Fig. 4a. The differing contrast might suggest that the particle is polycrystalline, but the SAD pattern indicates that the particle is single-crystal Si (Fig. 4b). When the interface is examined using HRTEM, the (111) lattice fringes truncate near the middle of the particle, as shown in Fig. 4c. Thus, approximately half of the particle is crystalline, while the other half is amorphous. The nature of this interface, and the above interpretation of Fig. 4c, may be examined by tilting the Si nanoparticle to different orientations. Fig. 5 shows a single incompletely solidified nanoparticle imaged on three different zone axes. There is little change in the appearance of the nanoparticle from the [001] to the [114] zone axis, while a significant change in contrast is observed from the [001] to the $[\bar{1}12]$ axes.

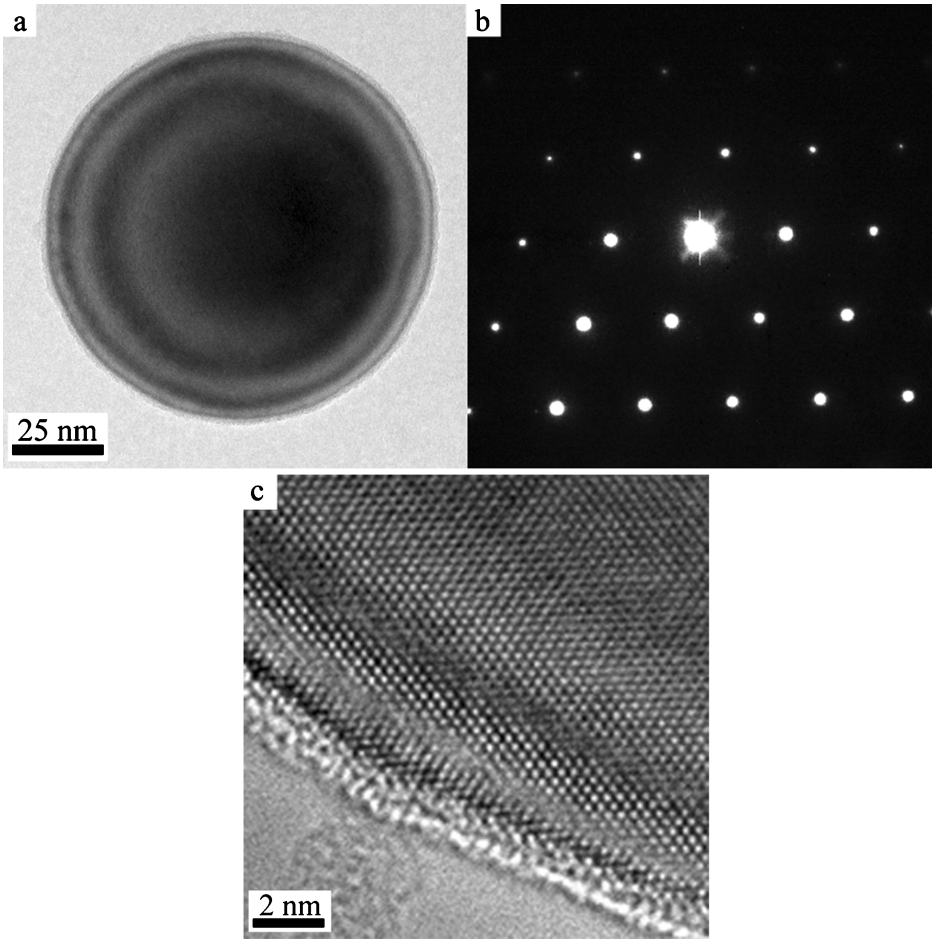


*Figure 1* TEM observations of a single-crystal Si nanoparticle. (a) is a bright-field (BF) TEM image of an individual Si nanoparticle. The symmetry of the thickness fringes implies that the nanoparticle is spherical in shape. (b) is a selected-area diffraction (SAD) pattern of the nanoparticle; the symmetry and spacing is consistent with the [011] zone of Si. The aberration-corrected HRTEM image in (c) shows the crystalline lattice in the [011] direction and the presence of an amorphous surface layer about 1 nm thick.

The Si particle in Fig. 6 combines a number of these observations. In the BF TEM image shown in Fig. 6, the particle appears as almost perfectly spherical in shape. However, the surface of the Si particle contains some faceted regions and the particle contains both a twin boundary and a stacking fault, denoted with black and white arrows in Fig. 6, respectively. The twin boundary proceeds through the particle as observed in Figs 2 and 3a The (111)-type stacking fault terminates on the twin boundary near the center of the particle. Most interesting is the presence of a relatively large amorphous droplet. Under the droplet, the surface of the Si particle has the opposite curvature.

Evidence of more significant faceting was observed for other nanoparticles. Fig. 7a shows a Ti nanoparticle that appears faceted for approximately half of its perimeter. Using the SAD pattern shown in Fig. 7b, these facets can be associated with specific crystallographic planes. These are noted schematically in Fig. 7c. It is notable that the shaded region in Fig. 7c does not contain any obvious faceting when compared to the remainder of the nanoparticle but instead maintains an appearance similar to that of an entirely spherical nanoparticle. HRTEM images of similarly faceted Ti nanoparticles show that the facets are not atomically flat. Fig. 8 shows the intersection of two larger facets on the surface of a Ti nanoparticle. This HRTEM image clearly shows that the surface of such faceted nanoparticles may be uneven; the change in height in Fig. 8 is approximately 5 nm.

Some particles were found to have undergone agglomeration and sintering processes during their formation. The BF TEM image in Fig. 9a shows two relatively spherical Ti particles that have formed a single particle. Each of these particles is single-crystal in nature as can be seen from their SAD patterns of 'P1' and 'P2' in Figs 9b and c, respectively. As can be seen from these diffraction patterns, the particles are aligned such that $[1\bar{2}10]_{P1}/[22\bar{4}0]_{P2}$ and $[10\bar{1}0]_{P1}/[0001]_{P2}$.

## 4. Discussion

Because of their inherently small size, the surface energy of a nanoscale structure can account for a significant

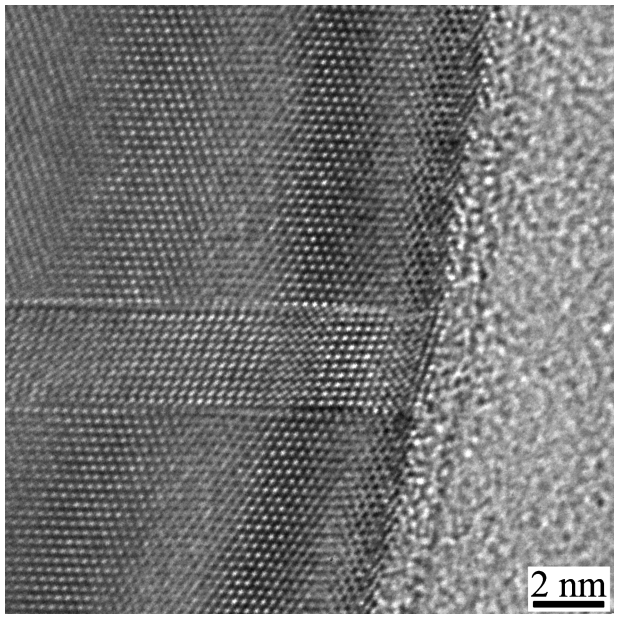


*Figure 2* An aberration-corrected HRTEM image of two (111) twin boundaries in a Si nanoparticle. The boundaries are approximately 2.5 nm apart, and are atomically flat. The twin domain exhibits a (111) facet at the surface of the nanoparticle.

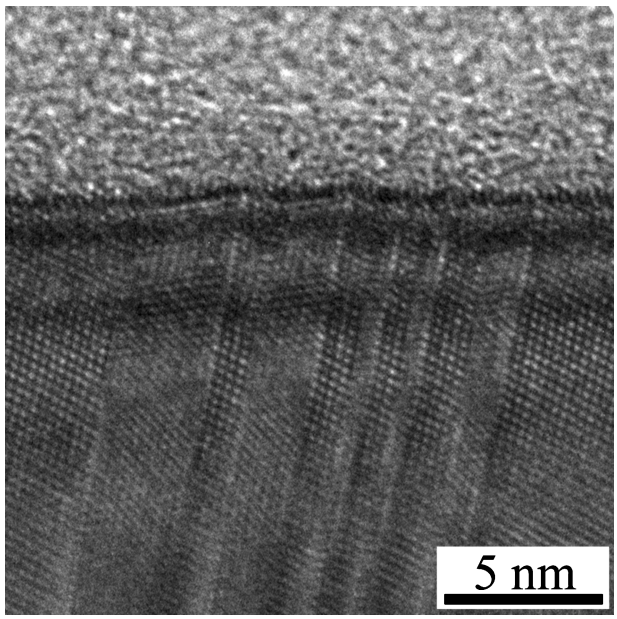


*Figure 3* A HRTEM image of nine (111) twin boundaries in a Si nanoparticle. These twin boundaries are irregularly spaced, but are atomically flat. (111) faceting is visible at the surface of the nanoparticle where the twins intersect the surface.

proportion of the total energy [1]. Thus, the benefits of minimizing the total surface energy are considerable for a nanoparticle which has a large surface area when compared to its volume. Providing kinetic processes allow it, small particles will adopt a shape which will accomplish this task [88]. As most solids are non-isotropic, this leads to the formation of facets that are surfaces of minimum surface energy. This study found two examples of faceting: between twin boundaries (Figs 2 and 3) and on the surface of some nanoparticles (Figs 6 and 7). The (111) faceting between the twin boundaries is small with respect to the diameter of the particle, with the average facet being around 0.8 nm long. The larger surface facets seen for the particles in Figs 6 and 7 can compose a significant portion of the surface. However, in each case a large percentage of the nanoparticle remained approximately spherical in shape, as was noted in Fig. 7c.

The overall spherical shape of the nanoparticles is characteristic of liquid droplets, which are isotropic and assume the shape of a sphere to minimize the total surface area; i.e., the shape minimizes the total surface energy of the droplet. The HPPD process involves very high velocities and thermal gradients for both the process gases and generated nanoparticles. The thermal gradients in the system have been calculated to be on the order of $10^7$ K/s, while the particles have a velocity of approximately 2000 m/s when they leave the nozzle [65–67, 73]. This combination of process parameters means that the Si nanoparticles are likely quenched rapidly from the liquid phase [35, 43]. The formation and growth of the nanoparticles occurs by coalescence in the liquid phase while the temperature is above the melting point of the material being produced. Other studies of particles generated in flames and plasmas have noted that short characteristic residence times lead to particles with a predominately spherical morphology [41, 89, 90].

The crystallization of the liquid spherical nanoparticles occurs very rapidly due to the large thermal gradients present in the HPPD system. Such rapid crystallization behavior has been observed for undercooled liquid droplets of Si, Ge, and Ni with diameters of several millimeters [51, 91–94]. The predominant mechanism for this solidification was found to be by the growth of dendrites into the liquid phase. The morphology of these dendrites, and consequently the shape of the CF, was dependent on the interfacial undercooling [63, 94]. The resulting solid spheres were single crystals and usually contained twin defects. These twin defects have been suggested to aid in the propagation of the solid dendrites by forming grooves at the CF, allowing for rapid atomic growth [94]. Similar behavior was found using spray atomization to produce rapidly solidified spherical particles of Al with diameters of $>$200 nm [60, 61].

The sintering of spherical particles has been studied in many systems on differing length scales [37, 95–103]. The appearance of particles such as those shown in Fig. 9 is similar to images of liquid-glass spheres that are in intermediate stages of sintering [104]. These two spherical constituent particles ($P_1$ and $P_2$) and the region of their overlap are shown schematically superimposed in Fig. 10. The diagram has been drawn assuming that the

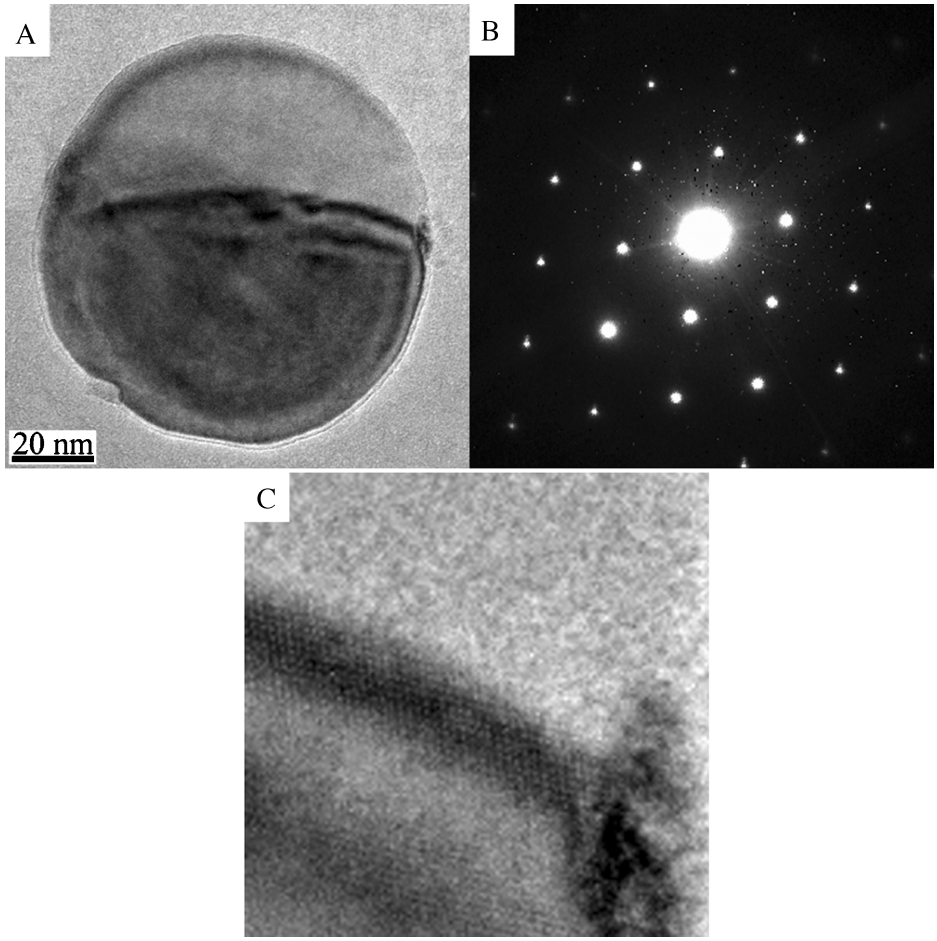


*Figure 4* TEM analysis of an incompletely crystallized Si nanoparticle. The BF TEM image in (a) exhibits a large contrast difference between the two halves of the nanoparticle. The [011] SAD pattern in (b) shows that this nanoparticle is single-crystal Si and not a polycrystalline agglomerate. At high magnifications in the HRTEM image of (c), the (111) lattice fringes can be seen to truncate at the contrast interface visible in (a). This implies that the lower half of the nanoparticle is crystalline Si, while the upper half is amorphous Si.

grain boundary which was formed at the initial contact has not moved even though the plane has changed as the 'groove' filled. The initial locations of the centers of the particles would be further apart as shown since they move together as sintering proceeds. The crystallographic alignment of the two particles implies that when the two particles came into contact, the temperature was still sufficiently high that they could rotate into a lower energy configuration. The fact that the particles are still spheres with little evidence for faceting provides, in principle, a method for comparing the kinetics of these two processes. Thus the interesting feature of this observation is that it implies that sintering took place very rapidly.

In this study, the presence of nanoparticles that had not completely crystallized provides some insights into the solidification processes for these small volumes. Specifically, because the nanoparticle can be observed in a non-dynamic environment (i.e., not in-situ during the solidification process) the shape of the CF can be more fully appraised. Investigations using high-speed cameras yield only a low-resolution, two-dimensional picture of the rapidly evolving crystal. In the TEM, multiple particles can be examined in different crystallographic orientations at atomic resolution. Generally speaking, the shape of the CF can be of three types: flat, convex, or concave. As can be seen by the thickness fringes in Figs 4 and 5, the interface is decidedly not flat. This leaves the latter two possibilities for the shape of the CF; these are schematically shown in Figs 11a and b, respectively. For each of these scenarios, the crystalline region spontaneously nucleates as the nanoparticle cools and the resulting CF progresses into the liquid. In both cases, the resulting nanoparticle is a spherical single crystal.

Additionally, both of these potential shapes of the CF can provide atomically flat twin boundaries. The flatness of the twin boundaries observed in this study implies that the twin is generated from a single point during solidification. The twin then propagates along the CF. One possibility is that the twin boundary will propagate normally to the CF, as shown for a convex CF in Fig. 12b.

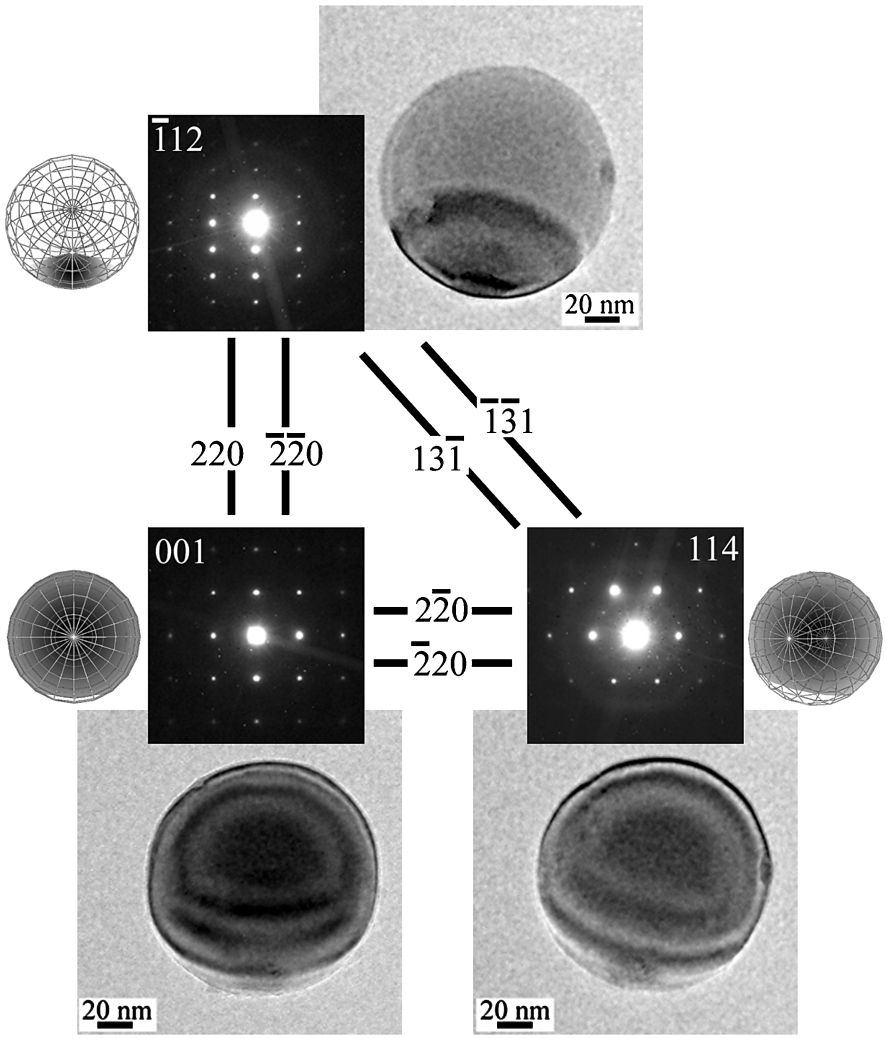


*Figure 5* Tilting experiment for an incompletely crystallized Si nanoparticle. Little change in the BF TEM image is seen upon tilting from the [001] to the [114] zone axis; however, there is a dramatic change in appearance moving from the [001] to the [$\bar{1}$12] zone axis. The relationship between these three zone axes is noted by the Kikuchi lines and schematic spheres between each image. The thickness fringes in the three BF images are consistent with a crystalline region with a convex boundary with the amorphous region of the particle.

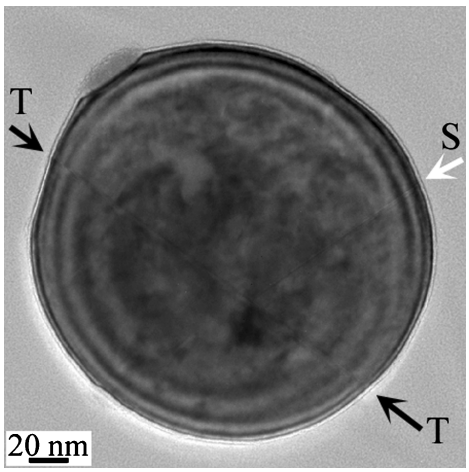


*Figure 6* BF TEM image of a Si particle with a 'droplet' of amorphous material on the surface. Additionally, this particle contains surface facets, a twin boundary (black arrows, T), and a stacking fault (white arrow, S) that intersects the twin.

This mechanism is also plausible for a concave CF. A second possibility for the generation of a twin is with the propagation of the defect parallel to the CF. This behavior is illustrated for a convex CF in Fig. 12a. Although the propagation of the twin occurs in two places, the singular nucleation of the twin ensures that the flatness of the twin boundary is maintained. Multiple twins may be generated in this way, leading to a structure similar to that seen in Figs 2 and 3. In comparison, it would be difficult for a concave CF to accomplish this, since the edges of the particle crystallize before the interior. Thus, a twin would have to be initiated on the opposite sides of the particle simultaneously and propagate towards each other to ensure flatness. This situation is unlikely, and supports the conclusion that the CF is convex. Multiple defects, such as those seen in Fig. 6, could easily be generated in a similar manner by nucleating along the convex CF as it progresses.

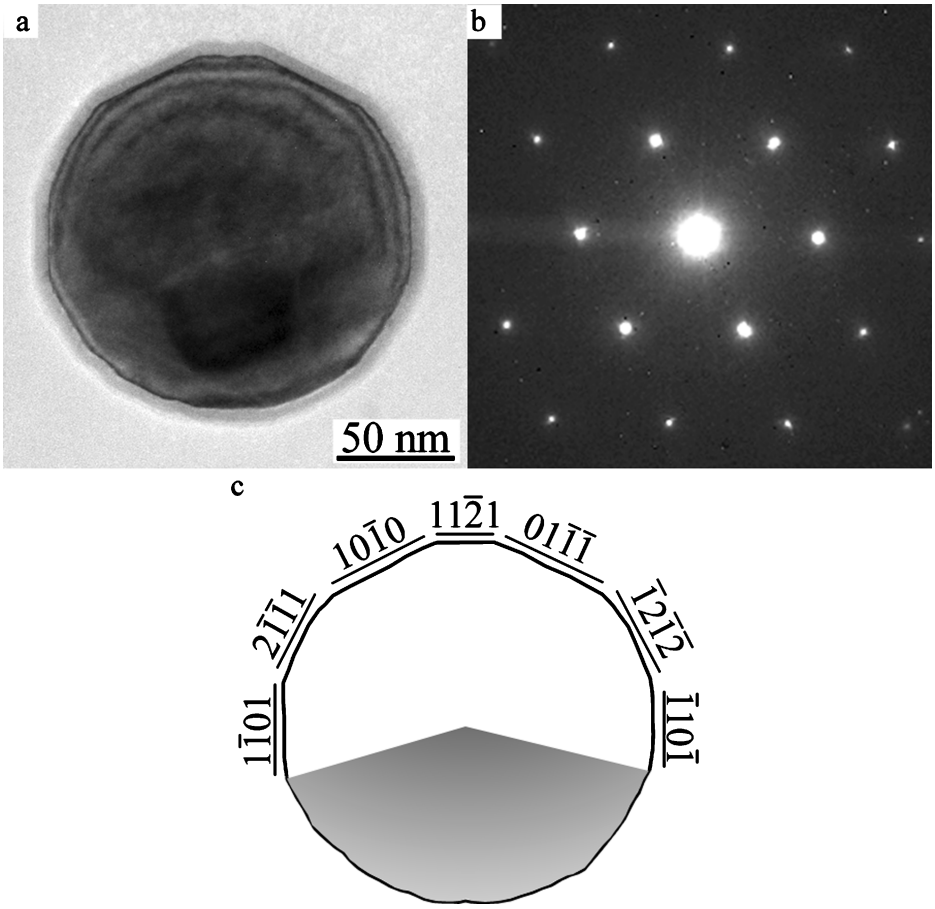


*Figure 7* (a) is a BF TEM image of a single-crystal Ti particle that exhibits faceting. Using the SAD pattern of this nanoparticle, as shown in (b), these facets may be associated with crystallographic planes in Ti. These facets are indexed and noted in (c). The bottom half of the particle maintains a spherical appearance and is shaded in (c).

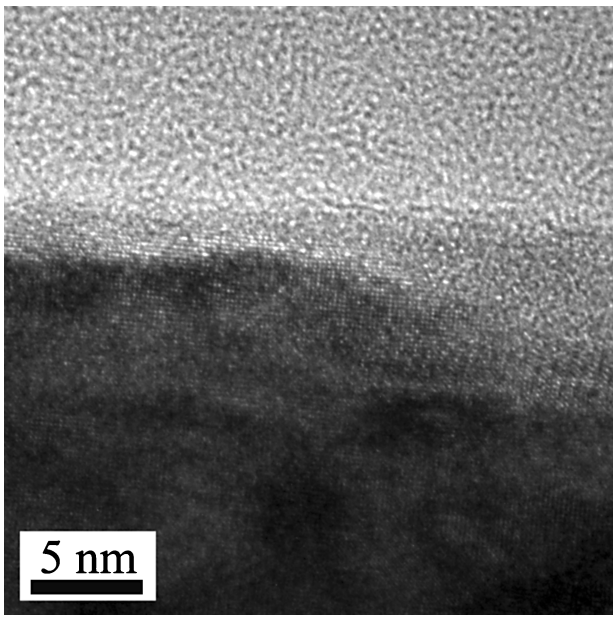


*Figure 8* HRTEM image of the surface of a faceted Ti nanoparticle. The uneven surface of the particle is evident.

Further insight into the shape of the CF is found by examining the symmetry of the thickness fringes in the incompletely solidified nanoparticles. The crystalline region of the Si nanoparticle in Fig. 4a contains thickness fringes that are indicative of a convex CF, but since this is only a single observation in a single direction, it is not unequivocal. It is notable that in the HRTEM image of Fig. 4c the surface of the particle seems to exhibit a surface groove. Such grooves are common in solid/liquid/vapor interfaces, and are studied to understand the dynamics of solidification and dewetting in other systems [105]. By tilting a similar particle to different zone axes, the shape of the CF may be better ascertained in three dimensions, as seen in Fig. 5. Although there is little change in the thickness fringes from the [001] to the [114] directions, there is a significant change moving to the [$\bar{1}$12] zone. If the physical rotation of the particle is considered along with the bright-field images, the thickness fringes indicate that the shape of the CF is indeed convex.

In addition to the observation of the shape of the CF, the tilting experiments have the additional benefit of illuminating the location of the crystalline nucleation point. For each liquid nanoparticle, the crystallization could begin

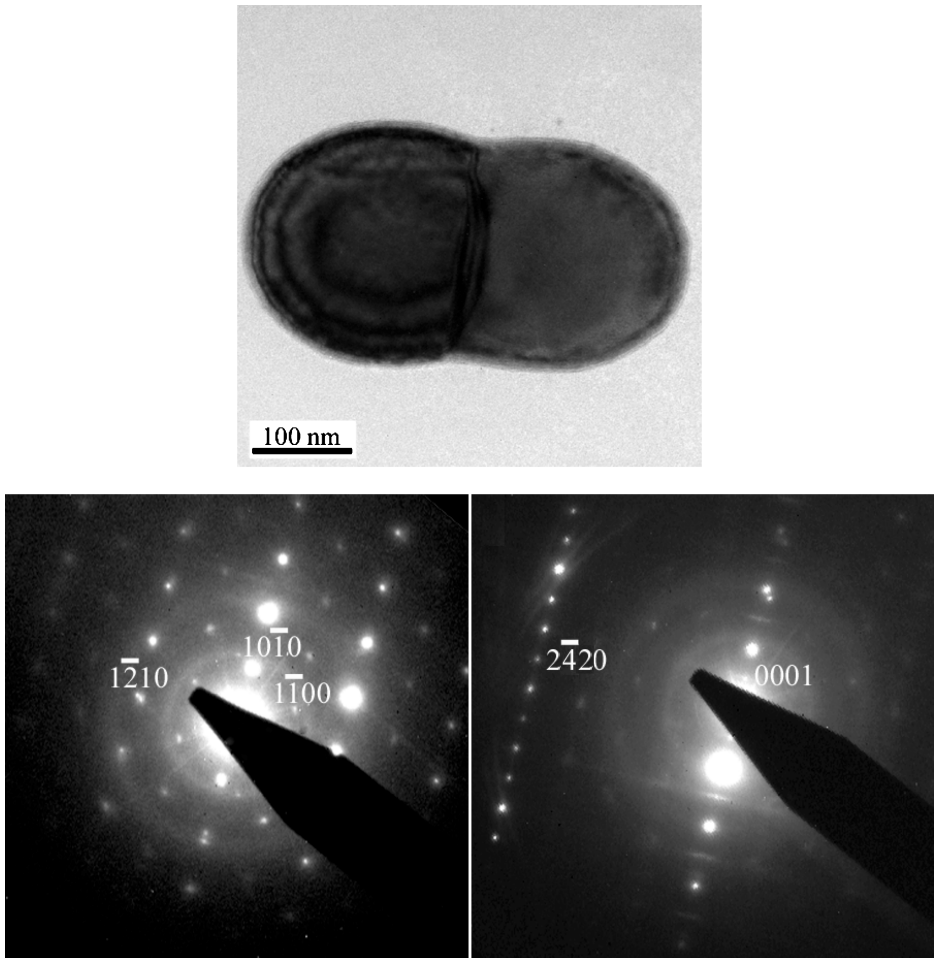


*Figure 9* (a) Bright-field TEM image of two Ti particles that have undergone a sintering process; the relative orientations of each constituent particle can be seen from their SAD patterns. The SAD pattern in (b) is from particle 'P1', while (c) is from particle 'P2.' This shows that $[1\bar{2}10]_{P1}/[2\bar{4}20]_{P2}$ and $[10\bar{1}0]_{P1}/[0001]_{P2}$ for these two particles.

either on the surface or in the interior of the nanoparticle. Examination of the images in Fig. 5 which were recorded at the [001] and [114] zones do not discriminate between either of these possibilities. However, by tilting the nanoparticle so that the electron beam is parallel to the $[\bar{1}12]$ zone, the crystalline region is in the location that is consistent with nucleation at the nanoparticle surface. This surface nucleation has also been observed in other rapid solidification processing work [106 ].

These findings are consistent with the earlier experimental observations of rapid crystallization in larger undercooled droplets [51, 60, 61, 91–94]. The shape of the CF does not appear dendritic or faceted, supporting the interpretation that the solidification occurred in the continuous growth regime. Additional factors contributing to this are the small size of the nanoparticles and the fact that the crystallization is spontaneous and not triggered by an outside seed crystal. It has been found that when larger droplets with diameters of $>200$ $\mu$m spontaneously crystallize, the dendritic behavior is much less prevalent [93]. Thus, the spherical nanoparticles crystal-

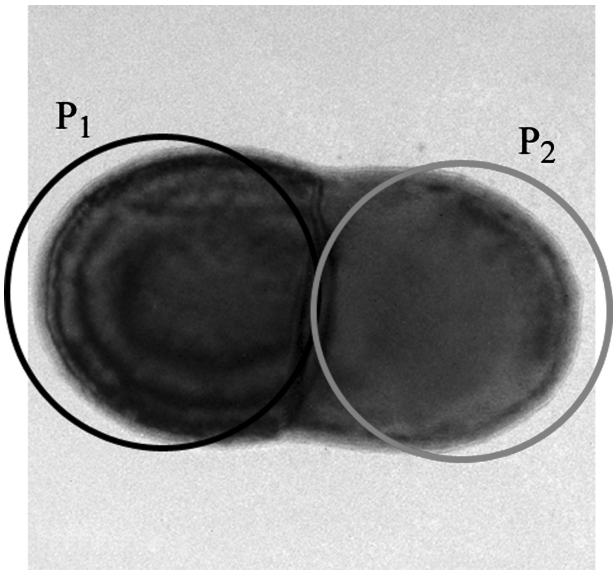


*Figure 10* The two spherical particles from Fig. 9, $P_1$ and $P_2$, with one possible location of the initial spheres (see text for discussion).

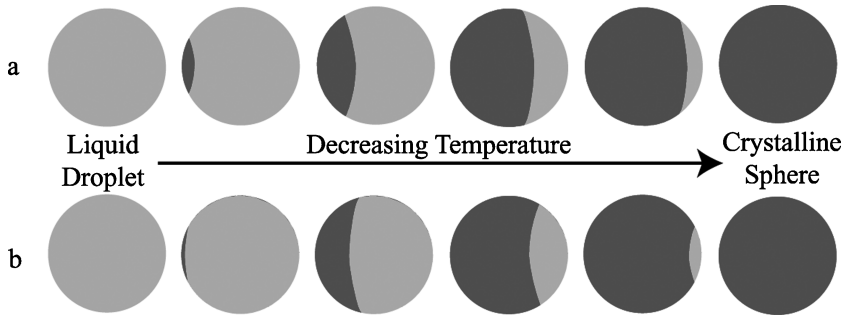


*Figure 11* Cross-section schematics of the crystallization of a liquid Si nanoparticle. In (a) the "crystallization front," or the boundary between the crystalline and amorphous regions, is a convex boundary, while in (b) the front is concave. The boundaries propagate across the nanoparticle as the temperature is decreased below the Si melting point, leaving a crystalline nanoparticle with a spherical shape.

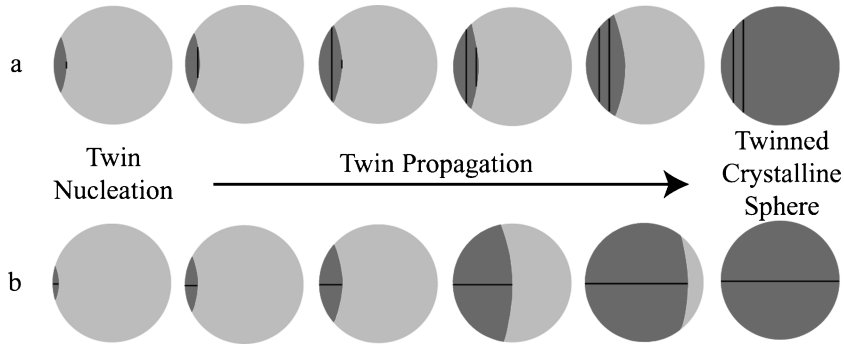


*Figure 12* Cross-section schematics showing the generation and propagation of twin defects for a convex crystallization front. In (a), multiple twin defects are generated and propagate normal to the front. In (b), a single twin defect is shown propagating parallel to the crystallization front. Both of these possibilities can generate atomically flat twin defects across the nanoparticle.

lize from only a single nucleus at the surface of the particle with a convex-shaped CF propagating into the liquid phase. Twin boundaries are readily generated as the particle solidifies and due to the speed and mechanism of the CF propagation these boundaries are atomically flat across the diameter of the particle. Even when multiple boundaries are closely spaced, there is no interaction or intersection of the twins. The twin boundaries may aid in the formation of the crystalline nanoparticles, as no incompletely crystallized nanoparticles were found that contained a twin boundary. In this case the nuclei may themselves be twinned favoring the geometry shown in Fig. 12b.

Droplets or protusions on the surfaces of large particles have been observed in previous studies of rapidly solidified Ge [51] and Al-Cu [61]. The size and extent of such features were found to be characteristic of certain ranges of undercooling for Ge [51]. It is possible that similar processes are occurring for the nanoparticles considered in this work; because of the highly dynamic environment in which the solidification occurs, some particles may be at a different degree of undercooling than others, leading to the formation of such 'droplets' or protrusions as seen in Fig. 6. As noted above, the droplet is not crystalline. As seen in Fig. 13, the curvature of the outer particle surface is smaller than for the Si particle as a whole, and that of the Si surface which is in contact with the 'droplet' has the opposite sign. The Si thickness fringes are essentially unaffected by the droplet. It is clear that this amorphous

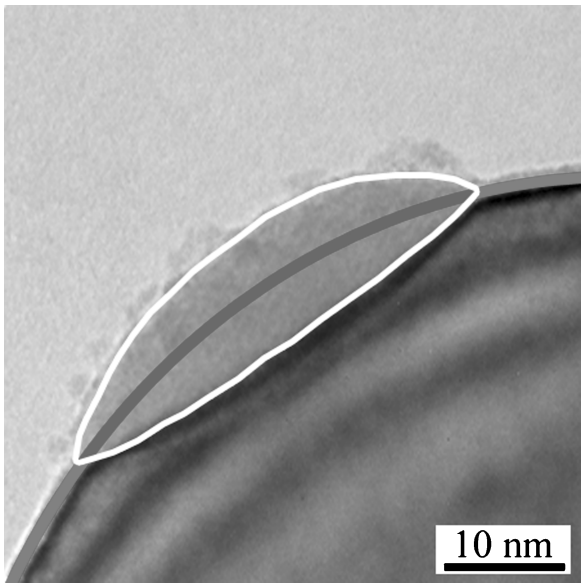


*Figure 13* The 'droplet' in Fig. 6 shown at higher magnification. The thick line defines the surface of the nanoparticle sphere; the lens-shaped region is the amorphous droplet.

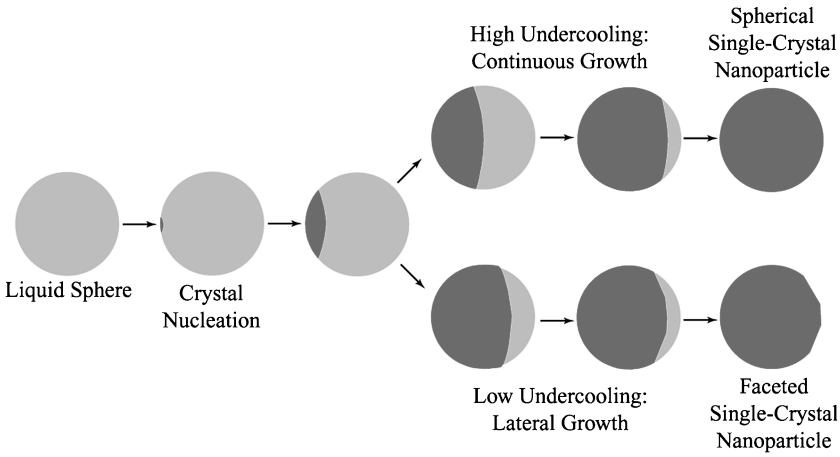


*Figure 14* Cross-section schematic detailing the progress of the crystallization front for the rapid solidification of spherical (top) and faceted nanoparticles (bottom). The morphological differences are likely due to the extent of undercooling of the nanoparticle as it solidifies.

region remained liquid (did not crystallize) as the nanoparticle cooled. In fact, its shape is strongly reminiscent of a liquid droplet in the surface of an immiscible liquid.

The observation of facets on the surfaces of some nanoparticles presents a challenge to the preceding discussion. Faceting may be found in anisotropic materials held at high temperatures, enabling atomic diffusion to the energetically favorable planes. However, if an initially spherical nanoparticle underwent such a process, the entire nanoparticle should appear faceted. As depicted in Fig. 7c, only parts of the nanoparticles exhibit such faceting, and the thickness fringes in the BF TEM images maintain that the remainder of the nanoparticle is spherical in shape (Figs 6a and 7a). Thus, these faceted nanoparticles contain evidence of undergoing crystallization in both the continuous and lateral growth regimes. This suggests that is possible to have a transition between these two growth regimes. This is schematically shown in Fig. 14. The liquid droplet is initially at a high degree of undercooling and the crystalline region nucleates at the surface of the nanoparticle and rapidly grows. As the heat of crystallization is liberated, the temperature of the droplet may increase [60]. If the heat is transferred away from the particle sufficiently quickly the droplet may continue with the continuous growth mechanism and lead to a spherical morphology. This would result in a nanoparticle similar in appearance to those shown in Figs 1–5. However, if the temperature of the droplet is raised sufficiently, the extent of undercooling is reduced, and lateral growth may result. This will change the shape of the CF from an atomically rough interface which progresses across the particle isotropically to a CF which becomes faceted and moves by the generation and propagation of crystallographic planes along the solid/liquid interface. This faceting of the CF has been simulated by Peteves and Abbaschian for Ge droplets [59] and by Levi and Mehrabian for Al droplets for diameters of $>100\ \mu$m [60]. When this faceted CF intercepts the surface of the liquid faceting of the nanoparticle surface would occur [107]. This would lead to a nanoparticle exhibiting traits of both growth regimes: a predominantly spherical appearance but with faceting on some of the surface of the nanoparticle. Additionally, this change in the extent of undercooling could lead to the formation of the 'droplet' observed in Fig. 6.

## 5. Conclusions

Hypersonic plasma particle deposition (HPPD), a thermal plasma process that uses large cooling rates, was used to deposit Si and Ti nanoparticles on TEM grids. These nanoparticles were observed to have a spherical morphology; such spheres were invariably single crystals. HRTEM analysis identified some nanoparticles to have atomically flat twin boundaries across the diameter of the particle; other nanoparticles are incompletely crystallized but still maintain the spherical morphology evident in fully crystalline particles. These results imply that the nanoparticles crystallized from a spherical liquid droplet as the material rapidly cools by the propagation of a "crystallization front." From an analysis of the geometry of the thickness fringes and twin boundaries in the TEM images, this front is likely convex in shape. Faceting of portions of the surface implies that a transition between the continuous and lateral growth mechanisms is possible during solidification. This transition is likely due to a reduction in the undercooling of the solidifying particle.

## Acknowledgments

This work has been supported by the NSF-NIRT program through grant NSF/DMI-0103169, by a Doctoral Dissertation Fellowship from the University of Minnesota and the 3M Heltzer Endowed Chair. Our colleagues in the University of Minnesota's HPPD program were extremely helpful, particularly J. Hafiz, X. Wang, and R. Mukherjee for discussions and for providing the material used in

this study. Additional discussions with W. Mook, W. W. Gerberich, J. V. R. Heberlein, S. L. Girshick, and P. H. McMurry are appreciated. Chris Nelson (National Center for Electron Microscopy), Markus Lentzen and Knut Urban (Reearcsh Center Jülich) were instrumental in obtaining the HRTEM results. The project on aberration correction of a transmission electron microscope was funded by the Volkswagen Stiftung.

## References

1. N. ICHINOSE, Y. OZAKI and S. KASHU, "Superfine Particle Technology" (Springer-Verlag, 1992).
2. M. C. ROCO, *J. Nanoparticle Res.* **3** (2001) 5.
3. H. GLEITER, *Prog. Mater. Sci.* **33** (1989) 223.
4. W. W. GERBERICH, W. M. MOOK, C. R. PERREY, C. B. CARTER, M. I. BASKES, R. MUKHERJEE, A. GIDWANI, J. V. R. HEBERLEIN, P. H. MCMURRY and S. L. GIRSHICK, *J. Mech. Phys. Solids* **51** (2003) 979.
5. W. W. GERBERICH and W. M. MOOK, *Pour la Science* **41** (2003) 19.
6. C. R. PERREY, W. M. MOOK, C. B. CARTER and W. W. GERBERICH, *Mater. Res. Soc. Symp. Proc.* **740** (2002) I3.13.1.
7. H. TAKAGI, Y. YAMAZAKI, A. ISHIZAKI and T. NAKAGIRI, *Appl. Phys. Lett.* **56** (1990) 2379.
8. C. J. MURPHY and J. L. COFFER, *Appl. Spectrosc.* **56** (2002) 16A.
9. L. ZHANG and D. XUE, *J. Mater. Sci. Lett.* **21** (2002) 1931.
10. L. M. ENG *Nanotechnology* **10** (1999) 405.
11. A. P. WEBER, M. SEIPENBUSCH, J. BINNIG and G. KASPER, *Particle & Particle Systems Charac.* **19** (2002) 300.
12. A. NAVROTSKY, *J. Therm. Anal. Calor.* **57** (1999) 653.
13. *Idem., J. Chem. Thermodyn.* **33** (2001) 859.
14. *Idem., J. Franklin Inst.* **340** (2003) 263.
15. L. WANG, K. VU, A. NAVROTSKY, R. STEVENS, B. F. WOODFIELD and J. BOERIO-GOATES, *Chem. Mater.* **16** (2004) 5394.
16. S. K. FRIEDLANDER, Smoke, Dust, and Haze "(Fundamentals of Aerosol Dynamics)," 2nd edn. (Oxford University Press Inc., 2000).
17. L. H. GERMER and A. H. WHITE, *Phys. Rev.* **60** (1941) 447.
18. H. J. WASSERMAN and J. S. VERMAAK, *Surf. Sci.* **22** (1970) 164.
19. C. R. BERRY, *Phys. Rev.* **88** (1952) 596.
20. C. CESARI, A. CHARAI and C. NIHOUL, *Ultramicroscopy* **18** (1985) 291.
21. S. J. DOUGLAS, L. ILLUM, S. S. DAVIS and J. KREUTER, *J. Colloid Interf. Sci.* **101** (1984) 149.
22. G. DRANSFIELD, In "Ceramic Technology International" edited by B. Ian, (Sterling, 1992) p. 71.
23. P. FAUCHAIS, E. BOURDIN, J. F. COUDERT and R. MCPHERSON, In "Topics in Current Chemistry (*Plasma Chemistry IV*)" edited by F. L. Boschke, (Springer, 1983) p. 59.
24. R. BINGHAM and V. N. TSYTOVICH, *IEEE Trans. Plasma Sci.* **29** (2001) 158.
25. H. HOFMEISTER, J. DUTTA and H. HOFMANN, *Mater. Sci. Forum* **235–238** (1997) 595.
26. A. C. XENOULIS, G. DOUKELLIS and T. TSAKALAOS, *NanoStructured Mater.* **10** (1998) 1347.
27. A. GARSCADDEN, *IEEE Conference Record—Abstracts* (1990) 118.
28. G. S. SELWYN, *Vide, les Couches Minces* **47** (1991) 129.
29. J. A. DURHAM, J. L. P. JR. and C. STEINBRUCHEL, *Microcontamination* **8** (1990) 37.
30. S. L. GIRSHICK and C.-P. CHIU, in "International Symposium on Combustion and Plasma Synthesis of High-Temperature Materials," (VCH Publishers Inc., Deerfield Beach, FL, San Francisco, CA, 1988) p. 349.
31. S. L. GIRSHICK and C.-P. CHIU, *Plasma Chem. Plasma Process* **9** (1989) 355.
32. W. D. KINGERY, H. K. BOWEN and D. R. UHLMANN, "Introduction to Ceramics" (John Wiley & Sons, 1976).
33. T. VESALA, M. KULMALA, R. RUDOLF, A. VRTALA and P. E. WAGNER, *J. Aerosol Sci.* **28** (1977) 565.
34. B. T. POE, P. F. MCMILLAN, D. C. RUBIE, S. CHAKRABORTY, J. YARGER and J. DIEFENBACHER, *Science* **276** (1997) 1245.
35. R. S. WINDLER, S. K. FRIEDLANDER and K. E. J. LEHTINEN, *Aerosol Sci. Tech.* **27** (1997) 191.
36. K. E. J. LEHTINEN and M. R. ZACHARIAH, *Mater. Res. Soc. Symp. Proc.* **731** (2002) W6.2.
37. M. R. ZACHARIAH and M. J. CARRIER, *J. Aerosol Sci.* **30** (1999) 1139.
38. R. C. FLAGAN and M. M. LUNDEN, *Mater. Sci. Eng. A* **A204** (1995) 113.
39. F. FABRY, G. FLAMANT and L. FULCHERI, *Chem. Eng. Sci.* **56** (2001) 2123.
40. C. G. GRANQVIST and R. A. BUHRMAN, *J. Appl. Phys.* **47** (1976) 2200.
41. E. BALABANOVA, *Vacuum* **58** (2000) 174.
42. *Idem., ibid.* **69** (2003) 207.
43. R. S. WINDLER, S. K. FRIEDLANDER and K. E. J. LEHTINEN, *Aerosol Sci. Tech.* **27** (1997) 174.
44. P. P. AHONEN, J. JOUTSENSAARI, O. RICHARD, U. TAPPER, D. P. BROWN, J. K. JOKINIEMI and E. I. KAUPPINEN, *Aerosol Sci.* **32** (2001) 615.
45. P. P. AHONEN, A. MOISALA, U. TAPPER, D. P. BROWN, J. K. JOKINIEMI and E. I. KAUPPINEN, *J. Nanoparticle Res.* **4** (2002) 43.
46. S. E. BATTERSBY, R. F. COCHRANE and A. M. MULLIS, *J. Mater. Sci.* **34** (1999) 2049.
47. D. LI and D. M. HERLACH, *Europhys. Lett.* **34** (1996) 423.
48. T. AOYAMA, Y. TAKAMURA and K. KURIBAYASHI, *Metall. Mater. Trans. A* **30A** (1999) 3013.
49. D. LI, K. ECKLER and D. M. HERLACH, *Acta Mater.* **44** (1996) 2437.
50. C. F. LAU and H. W. KUI, *J. Appl. Phys.* **67** (1990) 3161.
51. *Idem., Acta Metall. Mater.* **39** (1991) 323.
52. *Idem., ibid.* **41** (1993) 1999.
53. *Idem., ibid.* **42** (1994) 3811.
54. R. S. WAGNER, *Acta Metall.* **8** (1960) 57.
55. D. L. LI, T. VOLKMANN, K. ECKLER and D. M. HERLACH, *J. Crystal Growth* **152** (1995) 101.
56. D. LI and D. M. HERLACH. *J. Mater. Sci.* **32** (1997) 1437.
57. J. L. WALKER, In "Physical Chemistry of Process Metallurgy Part 2" edited by G. R. St. Pierre (Interscience Publishers, 1961) p. 845.
58. S. D. PETEVES and R. ABBASCHIAN, *Metall. Trans. A* **22A** (1991) 1259.
59. *Idem., ibid.* **22A** (1991) 1271.
60. C. G. LEVI and R. MEHRABIAN, *ibid.* **13A** (1982) 221.
61. *Idem., ibid.* **13A** (1982) 13.
62. T. Z. KATTAMIS and M. C. FLEMINGS, *Metall. Trans.* **1** (1970) 1449.
63. J. W. CAHN, W. B. HILLIG and G. W. SEARS, *Acta Metall.* **12** (1964) 1421.
64. D. B. WILLIAMS and C. B. CARTER, "Transmission Electron Microscopy" (Plenum Press, 1996).
65. N. P. RAO, H. J. LEE, M. KELKAR, D. J. HANSEN, J. V. R. HEBERLEIN, P. H. MCMURRY and S. L. GIRSHICK, *NanoStructured Mater.* **9** (1997) 129.
66. N. P. RAO, N. TYMIAK, J. BLUM, A. NEUMAN, H. J. LEE, S. L. GIRSHICK, P. H. MCMURRY and J. HEBERLEIN, *J. Aerosol Sci.* **29** (1998) 707.

67. A. NEUMAN, J. BLUM, N. TYMAIK, Z. WONG, N. P. RAO, W. GERBERICH, P. H. MCMURRY, J. V. R. HEBERLEIN and S. L. GERSHICK, *IEEE Trans. Plasma Sci.* **27** (1999) 46.
68. N. P. RAO, S. L. GIRSHICK, J. HEBERLEIN, P. H. MCMURRY, S. JONES, D. J. HANSEN and B. MICHEEL, *Plasma Chem. Plasma Processing* **15** (1995) 581.
69. N. P. RAO, B. MICHEEL, D. J. HANSEN, C. FANDREY, M. BENCH, S. L. GIRSHICK, J. HEBERLEIN and P. H. MCMURRY, *J. Mater. Res.* **10** (1995) 2073.
70. J. HAFIZ, X. WANG, R. MUKHERJEE, W. MOOK, C. R. PERREY, J. DENEEN, J. V. R. HEBERLEIN, P. H. MCMURRY, W. W. GERBERICH, C. B. CARTER and S. L. GIRSHICK, *Surface Coatings Tech.* **188–189** (2004) 364.
71. P. LIU, P. J. ZIEMANN, D. B. KITTELSON and P. H. MCMURRY, *Aerosol Sci. Tech.* **22** (1995) 293.
72. *Idem., ibid* **22** (1995) 314.
73. F. DIFONZO, A. GIDWANI, M. H. FAN, D. NEUMANN, D. I. IORDANOGLOU, J. V. R. HEBERLEIN, P. H. MCMURRY, S. L. GIRSHICK, N. TYMAIK, W. W. GERBERICH and N. P. RAO, *Appl. Phys. Lett.* **77** (2000) 910.
74. K. URBAN and M. LENTZEN, *Microsc. Microanal.* **8** (2002) 8.
75. M. LENTZEN, B. JAHNEN, C. L. JIA, A. THUST, K. TILLMANN and K. URBAN, *Ultramicroscopy* **92** (2002) 233.
76. C. L. JIA, M. LENTZEN and K. URBAN, *Science* **299** (2003) 870.
77. M. HAIDER, S. UHLEMANN, E. SCHWAN, H. ROSE, B. KABIUS and K. URBAN, *Nature* **392** (1998) 768.
78. C. R. PERREY, C. B. CARTER and M. LENTZEN, *Microsc. Microanal.* **9** (2003) 958.
79. C. R. PERREY, S. THOMPSON, M. LENTZEN, U. KORTSHAGEN and C. B. CARTER, *J. Non-Cryst. Solids* **343** (2004) 78.
80. S. THOMPSON, C. R. PERREY, C. B. CARTER, T. J. BELICH, J. KAKALIOS and U. KORTSHAGEN, *J. Appl. Phys.* **97** (2005) 034310.1.
81. C. R. PERREY, M. LENTZEN and C. B. CARTER, *Microsc. Microanal.* **9** (2003) 394.
82. C. R. PERREY, S. S. THOMPSON, M. LENTZEN, U. KORTSHAGEN and C. B. CARTER, *Mater. Res. Soc. Symp. Proc.* edited by R. Biswas, G. Ganguly, E. Schiff, R. Carius and M. Kondo, **808** (2004) A8.7.1.
83. M. A. O'KEEFE, C. J. D. HETHERINGTON, Y. C. WANG, E. C. NELSON, J. H. TURNER, C. KISIELOWSKI, J. O. MALM, R. MUELLER, J. RINGNALDA, M. PAN and A. THUST, *Ultramicroscopy* **89** (2001) 215.
84. M. LENTZEN, C. L. JIA and K. URBAN, *Microsc. Microanal.* **9** (2003) 932.
85. C.-L. JIA, M. LENTZEN and K. URBAN, *Ibid.* **10** (2004) 174.
86. C. R. PERREY, R. THOMPSON, C. B. CARTER, A. GIDWANI, R. MUKHERJEE, T. RENAULT, P. H. MCMURRY, J. V. R. HEBERLEIN and S. L. GIRSHICK, *Mater. Res. Soc. Symp. Proc.* **740** (2002) I4.6.1.
87. C. R. PERREY, C. B. CARTER, J. BENTLEY and M. LENTZEN, *Microsc. Microanal.* **9** (2003) 412.
88. C. HERRING, *Phys. Rev.* **82** (1951) 87.
89. K. E. J. LEHTINEN, R. S. WINDELER and S. K. FRIEDLANDER, *J. Colloid Interface Sci.* **182** (1996) 606.
90. K. E. J. LEHTINEN and M. R. ZACHARIAH, *Phys Rev. B* **63** (2001) 205402.1.
91. G. A. COLLIGAN and B. J. BAYLES, *Acta Metall.* **10** (1962) 895.
92. T. AOYAMA and K. JURIBAYASHI, *Acta Mater.* **48** (2000) 3739.
93. T. AOYAMA, Y. TAKAMURA and K. KURIBAYASHI, *Metall. Mater. Trans. A* **30A** (1999) 1333.
94. G. DEVAUD and D. TURNBULL, *Acta Metall.* **35** (1987) 765.
95. B. DAVIDOVITCH, D. ERTAS and T. C. HALSEY, *Phil. Mag.* **84** (2004) 1937.
96. J. DUTTA, H. HOFMANN, R. HOURIET, H. HOFMEISTER and C. HOLLENSTEIN, *Colloids Surfaces A: Physicochemical and Engineering Aspects* **127** (1997) 263.
97. J. R. GROZA, *NanoStructured Mater.* **12** (1999) 987.
98. P. ZENG, S. ZAJAC, P. C. CLAPP and J. A. RIFKIN, *Mater. Sci. Eng. A* **252** (1998) 301.
99. H. TANAKA, *J. Ceram. Soc. Japan* **105** (1997) 294.
100. *Idem., ibid.* **103** (1995) 138.
101. J. RUBIO, J. L. OTEO, M. VILLEGAS and P. DURAN, *J. Mater. Sci.* **32** (1997) 643.
102. M. O. PRADO, E. D. ZANOTTO and C. FREDERICCI, *J. Mater. Res.* **18** (2003) 1347.
103. R. MEYER, J. J. GAFNER, S. L. GAFNER, S. STAPPERT, B. RELLINGHAUS and P. ENTEL, *Phase Transitions* **78** (2005) 35.
104. J. J. B. WACHTMAN, "Ceramic Innovations in the 20th Century" (The American Ceramic Society, Westerville, OH, 1999) p. 307.
105. E. SAIZ, A. P. TOMSIA and R. M. CANNON, *Acta Mater.* **46** (1998) 2349.
106. A. K. SRIVASTAVA, *J. Mater. Sci. Lett.* **19** (2000) 1217.
107. R. P. LIU, T. VOLKMANN and D. M. HERLACH, *Acta Mater.* **49** (2001) 439.